Effects of Polycrystalline Cu Substrate on Graphene Growth by Chemical Vapor Deposition

Joshua D. Wood,[†,‡,§] Scott W. Schmucker,[†,‡] Austin S. Lyons,[†,§] Eric Pop,*[,†,‡,§] and Joseph W. Lyding*[,†,‡,§]

[†]Department of Electrical and Computer Engineering, [‡]Beckman Institute for Advanced Science and Technology, and [§]Micro and Nanotechnology Laboratory, University of Illinois at Urbana—Champaign, Urbana, Illinois 61801, United States

S *Supporting Information*

ABSTRACT: Chemical vapor deposition of graphene on Cu often employs polycrystalline Cu substrates with diverse facets, grain boundaries (GBs), annealing twins, and rough sites. Using scanning electron microscopy (SEM), electron-backscatter diffraction (EBSD), and Raman spectroscopy on graphene and Cu, we find that Cu substrate crystallography affects graphene growth more than facet roughness. We determine that (111) containing facets produce pristine monolayer graphene with higher growth rate than (100) containing facets, especially Cu-(100). The number of graphene defects and nucleation sites appears Cu facet invariant at growth temperatures above 900 °C. Engineering Cu to have (111) surfaces will cause monolayer, uniform graphene growth.

KEYWORDS: Graphene, copper, crystallography, CVD, EBSD, Raman
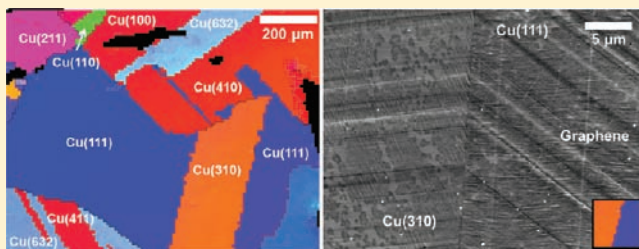
Mechanical exfoliation of graphene has enabled many fundamental studies of this novel material.[1] While most exfoliated samples are of high quality, the lateral dimensions are at most tens of micrometers, limiting the fabrication of consistent, wafer-scale graphene structures. To that end, techniques have been developed for the fabrication of large-area graphene samples by epitaxy on SiC[2] and by chemical vapor deposition (CVD) on catalytic metals like Ni[3−5] or Cu.[6] Graphene grown by CVD on Cu foils has generated interest due to low cost and the prospect of large-area monolayer coverage.[6] While these are promising characteristics, dendritic growth,[7] multilayer formation,[8] and lower carrier mobilities[6] than those of exfoliated samples[9] suggest sub-optimal quality of graphene grown on Cu. Lower quality likely results from heightened graphene nucleation and the formation of graphene grain boundaries (GBs) on the polycrystalline Cu substrates typically used, both of which are deleterious to transport.[10,11] The initial nucleation and growth dynamics of graphene play a critical role in determining the final film quality. However, such characteristics are dependent on Cu surface structure, suggesting that the underlying Cu substrate has a detailed influence on the nucleating carbon species during growth.[12,13]

In this study, we grow graphene by CVD on polycrystalline Cu foils with two carbon source gases, CH$_4$ and C$_2$H$_4$. We perform partial growths at 700 and 900 °C with C$_2$H$_4$ and full growths with CH$_4$ at 1000 °C. After high temperature processing the Cu surface contains many structures, namely, polycrystalline facets, grain boundaries, and annealing twins. We determine that the Cu(100) surface causes slow, multilayer graphene growth. High index Cu facets cause compact graphene island formation, but their growth rates are still faster than those on Cu(100).

In contrast, the Cu(111) surface promotes fast, monolayer graphene growth with few defects. It is therefore apparent that the Cu substrate influences graphene nucleation and growth significantly.

Previous work has suggested that the Cu—graphene interaction is relatively weak after growth[6,14] based on negligible copper carbide formation[15] and minimal graphene epitaxial alignment with the Cu substrate. Nevertheless, in early stages of graphene growth, the interaction between the carbon source and the Cu substrate becomes quite important. Low-energy electron microscopy (LEEM) studies have shown a preferred growth front for carbon species on the Cu(100) surface.[16] These results were corroborated indirectly by scanning tunneling microscopy (STM) studies through an in situ C$_2$H$_4$ decomposition process on both single crystal Cu(111)[12] and Cu(100).[13] However, most graphene growth by CVD on Cu is done with polycrystalline Cu foils, which have different growth transients and dynamics than single-crystal substrates.

To determine the crystal structure of our underlying Cu foil substrates, we perform electron-backscatter diffraction (EBSD) measurements. These measurements give us crystallographic orientation in the x, y, and z directions, but here we will only consider the z plane of the copper surface.[3,17] Figure 1 shows the partial growth of graphene at 700 °C with 20 sccm C$_2$H$_4$, 50 sccm H$_2$, and a 5 min growth time (30 s ramp up and fall times) on 5 mil thick (∼125 μm) Cu foil (Basic Copper, Carbondale, IL). Our growths employ lower flow rates of carbon-containing gas
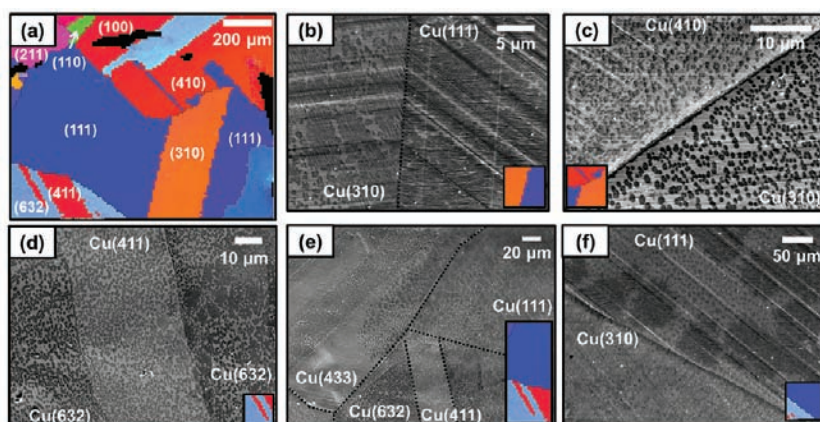
Figure 1. Scanning electron microscopy (SEM) imaging of graphene on different Cu facets. (a) Electron-backscatter diffraction (EBSD) image of a region of 5 mil Cu foil with graphene partially grown on it at 700 °C with C_2H_4. EBSD data show the underlying Cu crystal structure. (b) Graphene on two Cu grains, Cu(310) and Cu(111). The low-index facet Cu(111) has faster, dendritic graphene growth which spills into the neighboring Cu(310) facet. Cu(310) has compact graphene islands away from the boundary, and the black line indicates the Cu grain boundary (GB). (c) Cu(410)−Cu(310) GB, with graphene islands of differing size on either side. (d) Cu(632)−Cu(411)−Cu(632) twinning boundary, showing both islands and graphene overgrowth from the presence of neighboring Cu(111) facets. (e) Large area scan, indicating Cu(111) coverage. High-index planes show island formation. (f) Cu(111)−Cu(310) GB, showing large graphene islands near the boundary. Insets for (b−f) show EBSD data from (a) for the SEM regions.

with respect to the H_2 flow to decrease the chemical potential difference,[17] promoting crystallographic graphene edges[18] and monolayer growth.[8] An EBSD map of this foil shows a crystallographically diverse Cu surface, composed of Cu(111), Cu(310), Cu(410), Cu(411), Cu(632), Cu(211), Cu(110), and Cu(100) facets. The Cu(111) facet dominates the crystallographic map, which is expected as Cu(111) is the lowest energy Cu surface.[19]

Next, we correlate the EBSD map with scanning electron microscope (SEM) imaging to assess graphene coverage visually. In Figure 1b, we see nearly complete graphene coverage on the Cu(111) facet,[20] whereas its neighboring Cu(310) facet is not completely covered. Moreover, graphene growth on the Cu(111) facet appears to spill over into the Cu(310) facet (crystallographic cross section given in the Supporting Information), suggesting that the presence of the Cu(111) facet influences nearby growth dynamics. In the Supporting Information, we show how graphene preferentially nucleates on the Cu grain boundaries (GBs), consistent with predictions for Ni[3,5] and surface roughness based diamond nucleation.[21] As graphene starts to nucleate at the Cu GBs (e.g., the Cu(111)−Cu(310) GB) and grows faster on the Cu(111) surface, additional carbon molecules from the gas adsorb on the existing graphene−Cu(111), diffuse on the film, and make their way quickly to the film edges, where the Cu catalyst dehydrogenates them.[17,22] In these diffusion limited processes, graphene films on or near the Cu(111) surface appear dendritic, akin to STM studies of adsorbed atoms on Pt(111).[23] Similar dendrites were recently reported by LEEM of graphene on single-crystal Cu(111).[24]

Far from the Cu GB in Figure 1b, graphene forms compact islands on the Cu(310) surface, which is expected for surfaces not containing (111) terraces.[23] A higher island density will lead to a higher density of graphene GBs and adverse transport effects.[11,25] However, it has been suggested that at high temperature (∼1000 °C) the thermal energy is high enough to restructure compact islands and prevent formation of GBs where the islands meet.[26,27] Nevertheless, typical CVD growths have heightened

Cu sublimation at high growth temperature, Cu GB migration causing elongated graphene film formation,[28] and graphene wrinkles and ripples induced by thermal expansion.[29] These phenomena suggest that the dynamics of merging graphene islands is complex and is likely to form a chain of defects.[30]

Additional compact island formation is shown in Figure 1c for two high-index surfaces, Cu(410) and Cu(310). On these surfaces, hydrocarbons adsorb at certain preferential locations, such as point defects, surface kinks, adatom vacancies, or terrace steps.[31] At these sites, carbon species readily adsorb and dehydrogenate until the active Cu site is covered, terminating the reaction.[7,26] However, carbonaceous species have lowered carbon diffusion and dimerization on these surfaces,[20] making them less likely to propagate from the nucleation site. Hence, these sites have been called undersaturated or saturated, but not supersaturated,[32] which is necessary to propagate growth. While raising the growth temperature improves diffusion and can cause supersaturation, these sites' structure makes them temperature-invariant. The lack of supersaturation results in slower growth and defective,[18] multilayer graphene. Within panels c−e of Figure 1, the presence of Cu(111) terraces influences growth within the other high-index facets, such as Cu(411) or Cu(433). Graphene from Cu(111) can overgrow onto the high index surfaces before compact islands can form.

Nonetheless, SEM imaging is insufficient for characterization of graphene coverage, as higher contrast regions are not necessarily graphene. Furthermore, when discussing the matter of graphene supersaturation on Cu, it is important to see if higher growth temperature influences complete film coverage. To further examine the graphene film properties by Raman spectroscopy[33−35] and atomic force microscopy (AFM), we pattern raised mesas (∼20 μm high) on 1.4 mil Cu foil using standard photolithography. Two example mesas are shown optically by bright field imaging in panels b, d, and e of Figure 2. We grow graphene at 1000 °C with 850 sccm of CH_4 for the mesa of panels a and b of Figure 2. Additionally, we grow graphene at 1000 °C with 100 sccm of CH_4 for the mesa of panels c−f of Figure 2. Both growths use 50 sccm of
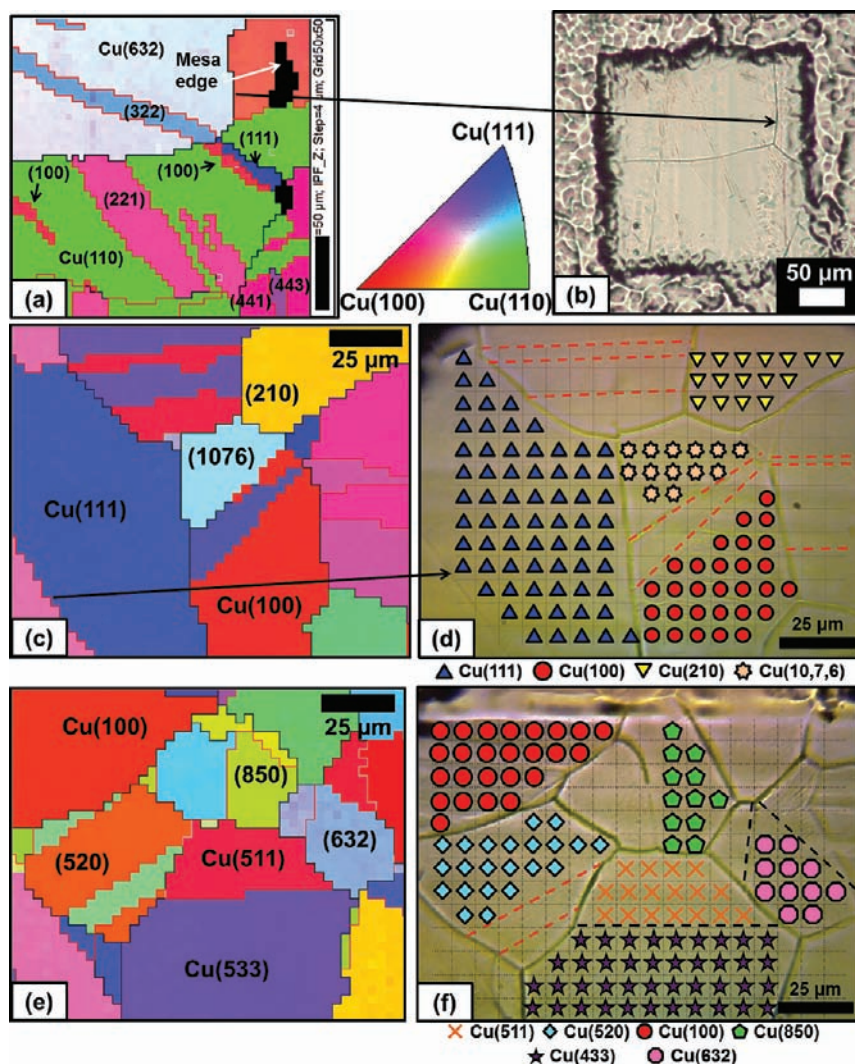
Figure 2. Defining Cu crystal structure and registry mesas for CVD graphene. (a) Electron backscatter diffraction (EBSD) of a Cu registry mesa shown optically in (b). EBSD black lines are copper grain boundaries, and EBSD red lines are annealing twins. Cu mesa is composed of many crystal facets. (c) EBSD and optical (d) information for another Cu mesa. The optical image of (d) shows the Raman spectra locations for different Cu facets, indicated by symbols (within the dotted lines). (e) Upper section of the Cu mesa in (c), showing high-index Cu facets. (f) Optical image of (e), with Raman spectra locations given by the symbols.

H_2 and a 30 min growth time. As before, we identify the Cu substrate facets by EBSD, indicated in panels a, c, and f of Figure 2. The two mesas are highly polycrystalline, as seen in the EBSD mosaic. We give schematics of the mesas' relevant facets in the Supporting Information, elucidating this high vicinality. The different shapes within the optical images of panels d and f of Figure 2 show Raman point spectra positions for the varying Cu facets.

To see whether nucleation and initial growth transients manifest themselves in the steady-state film, we perform spatially resolved Raman spectroscopy of fully grown graphene on Cu for the mesa in Figure 2d. Spatially resolved Raman spectra for the regions of panels b and f of Figure 2 are given in the Supporting Information. Within the optical image of Figure 3a, we identify the underlying Cu facets and annealing twins (red lines) using information from Figure 2c. Point Raman spectra of Figure 3b—taken at the points indicated by the shapes in Figure 3a—indicate more multilayer coverage[33−35] (intensity ratio $I_{2D}/I_G \sim 1.48$) on the Cu(100) surface and the high-index Cu(533) and Cu(10,7,6) surfaces ($I_{2D}/I_G \sim 1.93$ and $I_{2D}/I_G \sim 1.74$, respectively). On the

Cu(111) surface, the graphene coverage is high-quality monolayer ($I_{2D}/I_G \sim 4.16$). The D band, which normally assesses the graphene quality, is weak or nonexistent in these point spectra.

Analyzing the Raman intensity ratio I_{2D}/I_G (monolayer ratio) spatial map of Figure 3c, we see a lower monolayer ratio for the Cu(100) surface and larger ratios for the high-index surfaces and Cu(111). This suggests that the diffusion of carbon-containing species is slower on Cu(100) compared to the higher-index surfaces and Cu(111). Adatom diffusion on Cu(100) compared to Cu(111) has been studied previously,[36] with Cu(100) requiring surface atom exchange. Surface atom exchange is markedly slower than simple adatom hopping, which occurs on Cu(111). Thus, on Cu(100) surfaces, C atoms could stack in a multilayer configuration to lower surface[36] and adsorption energy.[17] Conversely, carbon's higher diffusion rate on Cu(111) will promote monolayer formation. The higher-index surfaces are composed of Cu(100), Cu(110), and Cu(111) monatomic terraces and steps, as discussed in the Supporting Information. We find that carbon diffusion and graphene growth on those surfaces is
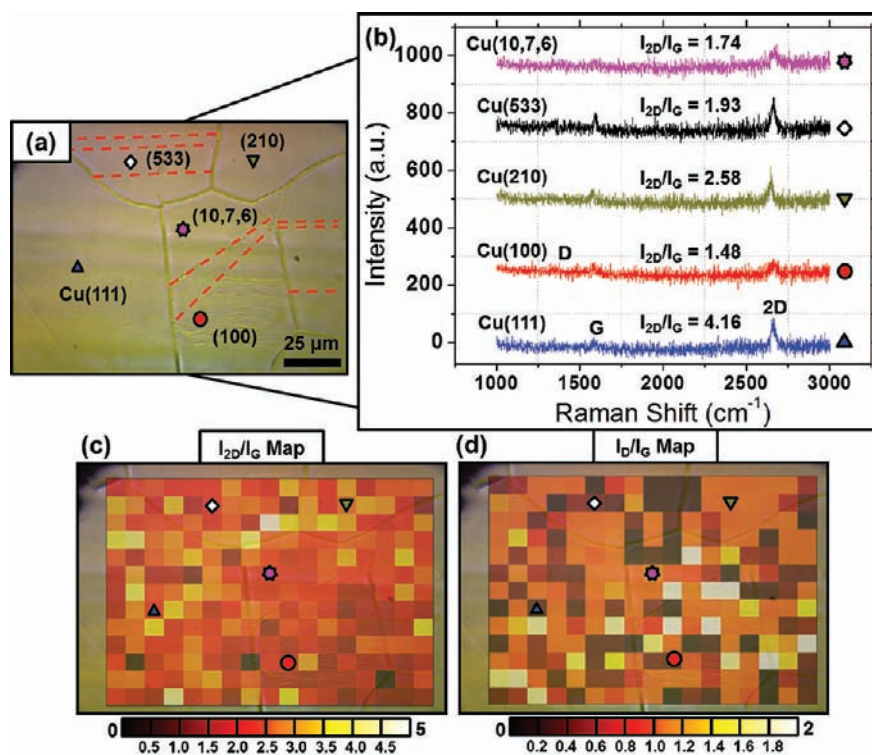
Figure 3. Reconciling graphene coverage with Cu facets by Raman spectroscopy. (a) Optical image of Cu mesa, with Cu crystal facets identified and annealing twins (dotted) present. Raman spectra taken at the colored shapes. (b) Raman point spectra of selected spots, with D, G, and 2D bands indicated. The graphene overall has few defects, but graphene on the Cu(100) has the lowest I_{2D}/I_G intensity ratio, indicative of few-layer growth. Cu(111) has pristine, monolayer graphene. (c) Raman spatial map of graphene monolayer intensity ratio I_{2D}/I_G for the region in (a). The Cu(100) surface as well as highly faceted regions like Cu(10,7,6) have lower monolayer intensity ratios, limited by carbon surface diffusion. (d) Graphene defect intensity ratio I_D/I_G for the same region. Defect distribution looks uniform, with differences due to Raman sampling of graphene nucleation sites. Raman pixel size is 7.5 μm at 633 nm excitation.

dependent on the percentage of Cu(111) surface present in the decomposed high-index facet. A high-index surface close to Cu(111) on the stereographic triangle, namely, with a high (111) percentage, will likely have a higher diffusion rate and predominantly monolayer graphene.

For the I_D/I_G (defect ratio) map of Figure 3d, the distribution looks more uniform across the mesa, with some sparse points differing from the norm. On the coarse scale of our Raman map ($\sim$100 μm by $\sim$130 μm), it is likely that these sparse points correspond to graphene nucleation centers.[37] These nucleation centers appear consistently across the different Cu crystals, regardless of whether they are low- or high-index surfaces. For the C_2H_4 partially grown graphene in panels b—f of Figure 1, it is evident that that high-index Cu surfaces cause compact island formation for initial graphene nucleation and ultimately slow down growth. However, higher graphene diffusion on Cu(111) confounds our ability to discern individual nucleation sites by SEM. It is therefore possible that both the low- and high-index facets would have similar nucleation densities but different growth rates, hiding the nucleation sites. It is more likely, however, that this nucleation difference is from both higher nucleation site adsorption energy on high-index surfaces and lower hydrocarbon cracking efficacy at the growth temperatures in Figure 1 (700 °C). At low temperature, the high probability of vicinal, high-index facets forming compact islands follows from this adsorption energy argument, resulting in denser nucleation. Moreover, for fully grown graphene at 750 °C, this was shown to lead to higher

disorder and smaller graphene domains.[38] Hydrocarbons at 1000 °C for the full graphene film of Figure 3d have high cracking efficacy and diffusion, leading to fewer nucleation sites and Cu facet invariance in I_D/I_G from carbon supersaturation.[32]

In Figure 4 we present a quantitative assessment of graphene coverage from the SEM images shown in Figure 1 and from the Raman analysis within Figure 3 and the Supporting Information. Figure 4a shows the I_{2D}/I_G monolayer ratio for all the Cu facets explored in Figure 3 and the Supporting Information. Overall, the distribution is monolayer-like and normal, peaked at $I_{2D}/I_G = 1.95 \pm 0.63$. However, the high standard deviation suggests some nonuniformity in the distribution due to the different Cu facets. Within panels b and c of Figure 4 we explore the defect ratio I_D/I_G shown in Figure 3d more carefully. In Figure 4b, we show I_D/I_G for partially grown graphene with 20 sccm C_2H_4 (5 min growth time) at 900 °C, whose value is $I_D/I_G = 0.67 \pm 0.48$ ($n = 174$). Conversely, the fully grown graphene sample from Figure 3 and the supplement has a value of $I_D/I_G = 0.69 \pm 0.47$ ($n = 436$), as Figure 4c indicates. We are unable to reject the null hypothesis at the 99% level suggesting that these samples may share a population. Similar hypothesis tests only supported the conclusion of differing populations at a statistically unreasonable 50% level. Compared to a full growth, partial graphene growths like Figure 4b should have more Raman active armchair edges[37] which contribute to a higher I_D/I_G value. While this changes the shape of the distribution relative to Figure 4c, the large sample size averages out these edge effects and points to a common
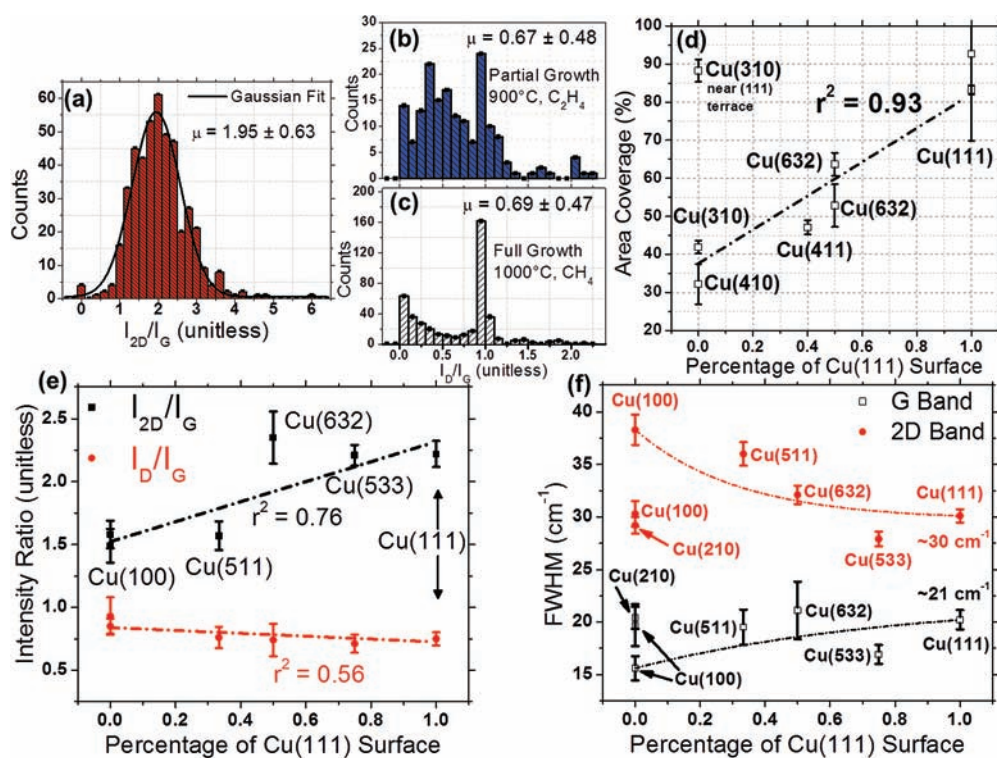
Figure 4. Quantitative assessment of graphene coverage. (a) Monolayer ratio (I_{2D}/I_G) histogram from Raman mapping for all Cu facets. Distribution is normal with a mean of $I_{2D}/I_G \sim 2$, expected for monolayer graphene. (b) Partially grown graphene defect ratio (I_D/I_G) histogram. Growth occurred at 900 °C with ethylene. (c) Fully grown graphene defect ratio (I_D/I_G) histogram, from the data in (a). The means and standard deviations of (b) and (c) are markedly similar, despite the partial growth. (d) Area coverage of facets containing the Cu(111) surface. More (111) surfaces have higher graphene coverage. These data are extracted from the SEM images in Figure 1. (e) Intensity ratios I_{2D}/I_G and I_D/I_G for different Cu facets. The independent variable gives the percentage of (111) terraces or steps in the facet. Cu(111) gives monolayer graphene, whereas the other facets give more multilayer coverage. Defect distribution appears invariant across the facets, indicating uniform nucleation and GB density. (f) 2D and G band full width at half maximum (fwhm) for different Cu facets from (e), with lines to guide the eye. Cu(100) and the higher index facets deviate from monolayer graphene value at $\sim$30 cm^{-1} for the 2D band. Further, they have a lower G band fwhm, highlighting substrate doping and strain in the graphene. Raman spectra collected at 633 nm excitation, 50× objective, and $\sim$9 mW power.

source for the I_D/I_G value. Our results suggest that this source is substrate invariant nucleation sites, as argued by a recent work.[27]

From contrast differences in the SEM images of panels b−f of Figure 1, we extract the amount of graphene area coverage following a procedure detailed in the Supporting Information. Figure 4d gives this area coverage as a percentage of the Cu(111) surface, which we determine by decomposing high-index facets into a superposition of (111), (110), and (100) facets. Surfaces containing (111) terraces—like Cu(411), Cu(632), and Cu(111)—show a linear increase in graphene coverage for the same growth time (5 min) when compared to surfaces with only (100) terraces (e.g., Cu(410), Cu(310)). In the case where surfaces were spatially near (111) terraces, like the Cu(310) surface near Cu(111) in Figure 1b, the heightened carbon diffusion on Cu(111) allowed graphene overgrowth into the Cu(310) facet, raising the area coverage on that facet. The Cu(632) surface contains both (111) and (100) facets, giving a larger overall area coverage than (100) containing surfaces alone, but less than surfaces with a larger percentage of (111).

Panels e and f of Figure 4 give Raman spectroscopic measurements (I_{2D}/I_G, I_D/I_G, 2D fwhm, and G full width at half maximum (fwhm)) of the regions assessed in panels a−c of Figure 4 obtained using 633 nm laser excitation and $\sim$9 mW power. Supplementary Tables S1−S3 in the Supporting Information present a full tabulation of these measurements with

sample numbers. Figure 4e details the monolayer (I_{2D}/I_G) and defect (I_D/I_G) ratios for different Cu facets as a percentage of the Cu(111) surface, as in Figure 4d. The intensity ratios for a particular facet are comprised of an entire population of point Raman spectra at the positions indicated in panels d and f of Figure 2. We note that graphene grown on Cu(111) is primarily monolayer with low defect density. The other facets appear more multilayer, especially Cu(100) ($I_{2D}/I_G \sim 1.5$). Error bars represent standard error of the mean. Surfaces which contain (111) terraces therefore have more monolayer graphene than those with (100) terraces. We ascribe this to a better lattice match of hexagonal graphene with the hexagonal Cu(111), promoting higher adsorption of carbon-containing species[17] and giving a quasi-epitaxial relationship, as was observed by STM.[12] Conversely, we attribute multilayer regions on Cu(100) to slow, adatom-exchange mediated carbon diffusion[39] and heighted atomic carbon adsorption energy,[17] as evident from the area coverage of Figure 4d. Interestingly, the I_D/I_G ratio is invariant across the facets listed. As is the case with panels b and c of Figure 4, we attribute this to common nucleation densities across the different facets. While Cu(100) gives relatively more defective graphene than Cu(111), in agreement with recent STM results,[13] there is insufficient statistical evidence to claim a crystalline influence on the number of graphene defects. On the basis of the results shown in Figure 4, at growth temperatures
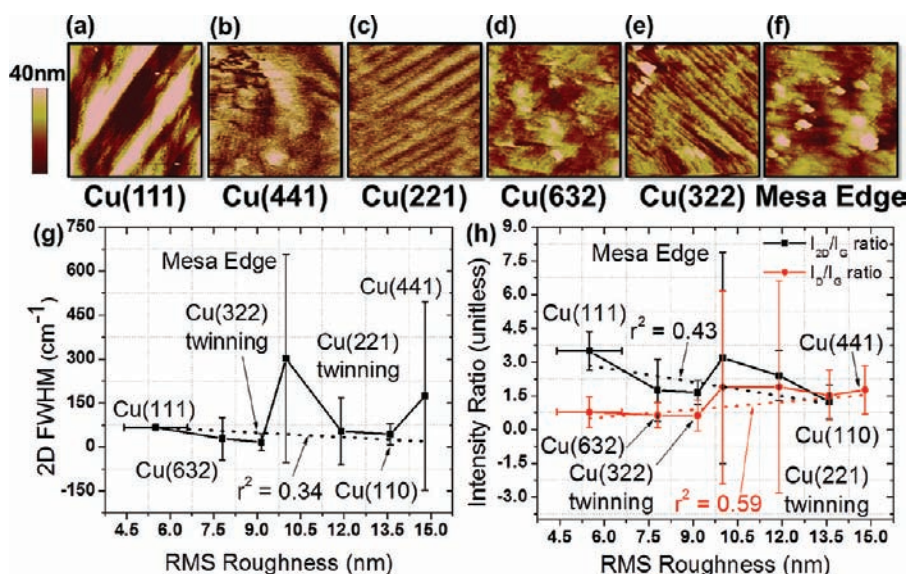
Figure 5. Root mean square roughness effects on graphene nucleation and quality. (a−f) 5 μm by 5 μm atomic force microscopy (AFM) images of the Cu(111), Cu(441), Cu(221), Cu(322), and Cu(632) facets, as well as the edge of the lithographically defined mesa. (g) AFM determined root-mean-square (rms) roughness and 2D peak full width at half-maximum (fwhm) values for different facets. Within the error, there is no apparent fwhm dependence on rms roughness. Average 2D fwhm is ∼56 cm^{-1}, higher than ∼30 cm^{-1} for graphene on SiO$_2$ due to Cu substrate doping and strain. (h) I_{2D}/I_G (graphene coverage) and I_D/I_G (graphene quality) ratios with respect to the rms roughness from (a−f), showing no dependence on roughness.

above 900 °C carbonaceous species do not preferentially nucleate on kinks, vacancies, and Cu GBs, unlike low temperature growth at 700 °C.

In Figure 4f, we show the 2D and G fwhm as a function of the facet Cu(111) percentage. The 2D band fwhm for exfoliated graphene is an indicator of the graphene layer number,[33,34] whereas the G band fwhm indicates doping,[40] strain,[41] and layer number. For surfaces with a higher percentage of Cu(111), the 2D fwhm approaches ∼30 cm^{-1}, consistent with monolayer graphene.[34] Graphene on Cu(100) has a 2D fwhm of ∼38 cm^{-1}, close to 40 cm^{-1} for turbostratically stacked multilayer graphene.[42] It is likely that graphene grown on Cu has been doped or strained due to its Cu underlayer,[12] and it is possible that these effects change with respect to the underlying facet. Using the Cu workfunction $\Phi_{Cu} \sim$ 4.7 eV and graphene workfunction $\Phi_G \sim$ 4.5 eV,[43] we estimate that the doping-induced shift in the fwhm of the G peak is ∼6 cm^{-1} with $E_F \sim$ 0.2 eV in the graphene.[44] Adding this to the known G fwhm[40] of 15 cm^{-1} gives an expected fwhm of ∼21 cm^{-1} for p-doped graphene on Cu. The G fwhm approaches this value on the Cu(111) surface and is lower on high-index surfaces and Cu(100) due to doping and G peak phonon stiffening.[40] Since the presence of the graphene overlayer strains the Cu, forming stepped surfaces[12,27] and hillocks,[16] it is possible that the Cu strains the conformal graphene as well, thereby contributing to G fwhm shift by strain.[41] However, the strain required to produce this shift would break the graphene, and we conclude that these facets also mainly dope the graphene.

Nevertheless, we must consider the possibility that the reduced surface roughness of Cu(111) and (111) containing surfaces could be the origin of this high-quality graphene growth. In Figure 5, we investigate the effects of Cu facet root-mean-square (rms) surface roughness on graphene nucleation and quality. Panels a−f of Figure 5 show 5 × 5 μm AFM images of different Cu facets. Figure 5a is an AFM image of the partially grown graphene on Cu(111) analyzed in Figure 1. Panels b−f of Figure 5 are AFM images of the fully grown graphene in Figures 2

and 3, respectively. The Cu foil of Figure 5a is wrinkled, giving the bright undulations apparent in the AFM image. We take rms roughness measurements within those regions and report the error for ensemble rms roughness. Conversely, rms roughness measurements for Panels b−f of Figure 5 are taken for the entire AFM image, without a statistical sampling that would allow an error bar in the rms measurement. We then plot the Raman 2D band fwhm and intensity ratios I_{2D}/I_G and I_D/I_G with respect to the facet rms roughness in panels g and h of Figure 5. It is apparent that the trend between the graphene quality metrics and the roughness is weak. A linear fit of the 2D fwhm against the rms roughness gives a Pearson correlation coefficient $|r|$ = 0.58, suggesting that there is no correlation between the 2D fwhm and rms roughness at 99% statistical significance. Furthermore, linear fitting the intensity ratios I_{2D}/I_G and I_D/I_G give $|r|$ = 0.81 and $|r|$ = 0.74, respectively, which are not correlated with rms roughness at 99% significance. This supports the notion that the rms roughness does not play a critical role in monolayer graphene growth quality. Hence, it is likely that that Cu crystallinity is playing a stronger role in the initial growth dynamics and eventual steady-state graphene film.

We have also examined the oxidation of our graphene-coated Cu foils. For instance, previous work[45] had reported oxidation resistance in ambient environments up to 200 °C; however here we found that the degraded graphene quality on Cu facets causes Cu oxidation at lower temperatures. The Cu begins to oxidize at 135 °C, with thicker CuO forming at higher temperatures as shown by optical images in the Supporting Information (full oxidation at 275 °C). The graphene film was only partially grown on the Cu foil; thus, it is possible that oxygen atoms are diffusing under the graphene to oxidize the Cu and oxidizing the Cu between the small graphene islands. However, subsurface oxidation is unexpected considering the low permeability of atoms under graphene.[46] Oxidation might be explained by oxygen etching of graphene edges[47] and GBs. In the latter case, a higher level of compact island formation—occurring on high-index

surfaces—will lead to more GBs. Consequently, those films will likely oxidize first. It is still possible that the exposed Cu is oxidizing and the graphene-coated regions are not oxidized. However, when we reduce the oxide by immersing the CuO foil into concentrated acetic acid for ~5 min and then reoxidize it, we find that this reoxidized film has a lower oxidation temperature, with full oxidation at 225 °C. Further, Raman spectra show high amorphous carbon coverage, suggesting that we damaged the original graphene film during oxidation.

In summary, we find that the growth of high-quality, large-domain graphene depends on the underlying Cu crystal structure. By EBSD, we determine that the Cu foils used in typical CVD growth are highly polycrystalline, containing Cu GBs, annealing twins, and high-index crystal facets. Low-index Cu facets produce more monolayer graphene with fewer defects as compared to the high-index surfaces. Raman spectroscopy shows that the Cu(111) surface grows the highest quality monolayer graphene, with high area coverage and short growth time. We attribute this to high diffusion[12,13] and improved adsorption[17] of carbon-containing species on Cu(111). The dendritic arms that we observe in our SEM images are consistent with molecular adsorption on face-centered cubic (111) surfaces.[23] Conversely, high-index facets form compact graphene islands based on lowered diffusion, nucleation, and pinning at rough surface sites, like step edges, adatom vacancies, and terrace kinks. Since Cu(111) is the lowest-energy Cu surface,[19] longer pregrowth anneals under Ar/H$_2$ flow at ~900 °C can help in the production of Cu(111) facets on the polycrystalline Cu substrate while mitigating Cu sublimation and GB migration.[28] Moreover, careful, high vacuum evaporation of single-crystal Cu(111) on basal-plane sapphire[48] might be another means by which to take advantage of the improved graphene growth qualities of Cu(111).

■ ASSOCIATED CONTENT

ⓢ Supporting Information. Experimental methods and discussion, graphene metrics as function of a surface's (100) percentage, additional spatial Raman spectroscopy for fully and partially grown graphene on Cu, Raman histograms for graphene metrics, SEM images of nucleated graphene, graphene coverage extraction method, optical images of graphene-coated Cu oxidation, and a table including all the parameters used in the Raman analysis. This material is available free of charge via the Internet at http://pubs.acs.org.

■ AUTHOR INFORMATION

Corresponding Author
*E-mail: epop@illinois.edu and lyding@illinois.edu.

■ ACKNOWLEDGMENT

■ REFERENCES

(1) Neto, A. H. C.; Guinea, F.; Peres, N. M. R.; Novoselov, K. S.; Geim, A. K. *Rev. Mod. Phys.* **2009**, *81* (1), 109.

(2) Emtsev, K. V.; Bostwick, A.; Horn, K.; Jobst, J.; Kellogg, G. L.; Ley, L.; McChesney, J. L.; Ohta, T.; Reshanov, S. A.; Röhrl, J. *Nat. Mater.* **2009**, *8* (3), 203–207.

(3) Gao, J.; Yip, J.; Zhao, J.; Yakobson, B. I.; Ding, F. *J. Am. Chem. Soc.* **2011**, *133* (13), 5009–5015.

(4) Kim, K. S.; Zhao, Y.; Jang, H.; Lee, S. Y.; Kim, J. M.; Kim, K. S.; Ahn, J.-H.; Kim, P.; Choi, J.-Y.; Hong, B. H. *Nature* **2009**, *457* (7230), 706–710.

(5) Zhang, Y.; Gomez, L.; Ishikawa, F. N.; Madaria, A.; Ryu, K.; Wang, C.; Badmaev, A.; Zhou, C. *J. Phys. Chem. Lett.* **2010**, *1* (20), 3101–3107.

(6) Li, X.; Cai, W.; An, J.; Kim, S.; Nah, J.; Yang, D.; Piner, R.; Velamakanni, A.; Jung, I.; Tutuc, E.; Banerjee, S. K.; Colombo, L.; Ruoff, R. S. *Science* **2009**, 1312–1314.

(7) Li, X.; Magnuson, C. W.; Venugopal, A.; Tromp, R. M.; Hannon, J. B.; Vogel, E. M.; Colombo, L.; Ruoff, R. S. *J. Am. Chem. Soc.* **2011**, *133* (9), 2816–2819.

(8) Bhaviripudi, S.; Jia, X.; Dresselhaus, M. S.; Kong, J. *Nano Lett.* **2010**, *10*, 4128–4133.

(9) Dorgan, V. E.; Bae, M.-H.; Pop, E. *Appl. Phys. Lett.* **2010**, *97*, 082112.

(10) Kim, K.; Lee, Z.; Regan, W.; Kisielowski, C.; Crommie, M. F.; Zettl, A. *ACS Nano* **2011**, *5* (3), 2142–2146.

(11) Huang, P. Y.; Ruiz-Vargas, C. S.; van der Zande, A. M.; Whitney, W. S.; Levendorf, M. P.; Kevek, J. W.; Garg, S.; Alden, J. S.; Hustedt, C. J.; Zhu, Y.; Park, J.; McEuen, P. L.; Muller, D. A. *Nature* **2011**, *469* (7330), 389–392.

(12) Gao, L.; Guest, J. R.; Guisinger, N. P. *Nano Lett.* **2010**, *10* (9), 3512–3516.

(13) Zhao, L.; Rim, K. T.; Zhou, H.; He, R.; Heinz, T. F.; Pinczuk, A.; Flynn, G. W.; Pasupathy, A. N. *Solid State Commun.* **2011**, *151* (7), 509–513.

(14) Giovannetti, G.; Khomyakov, P. A.; Brocks, G.; Karpan, V. M.; van den Brink, J.; Kelly, P. J. *Phys. Rev. Lett.* **2008**, *101* (2), 026803.

(15) Esconjauregui, S.; Whelan, C. M.; Maex, K. *Carbon* **2009**, *47* (3), 659–669.

(16) Wofford, J. M.; Nie, S.; McCarty, K. F.; Bartelt, N. C.; Dubon, O. D. *Nano Lett.* **2010**, *10*, 4890–4896.

(17) Zhang, W.; Wu, P.; Li, Z.; Yang, J. *J. Phys. Chem. C* **2011**, *115* (36) 17782–17787.

(18) Vlassiouk, I.; Regmi, M.; Fulvio, P.; Dai, S.; Datskos, P.; Eres, G.; Smirnov, S. *ACS Nano* **2011**, *5* (7), 6069–6076.

(19) Chatain, D.; Ghetta, V.; Wynblatt, P. *Interface Sci.* **2004**, *12* (1), 7–18.

(20) Chen, H.; Zhu, W.; Zhang, Z. *Phys. Rev. Lett.* **2010**, *104* (18), 186101.

(21) Pehrsson, P. E.; Glesener, J.; Morrish, A. *Thin Solid Films* **1992**, *212* (1–2), 81–90.

(22) Li, Z.; Wu, P.; Wang, C.; Fan, X.; Zhang, W.; Zhai, X.; Zeng, C.; Li, Z.; Yang, J.; Hou, J. *ACS Nano* **2011**, *5* (4), 3385–3390.

(23) Zhang, Z.; Lagally, M. G. *Science* **1997**, *276* (5311), 377–383.

(24) Nie, S.; Wofford, J. M.; Bartelt, N. C.; Dubon, O. D.; McCarty, K. F. *arXiv:1107.1909* **2011**

(25) Yazyev, O. V.; Louie, S. G. *Nat. Mater.* **2010**, *9* (10), 806–809.

(26) Li, X.; Cai, W.; Colombo, L.; Ruoff, R. S. *Nano Lett.* **2009**, *9* (12), 4268–4272.

(27) Rasool, H. I.; Song, E. B.; Allen, M. J.; Wassei, J. K.; Kaner, R. B.; Wang, K. L.; Weiller, B. H.; Gimzewski, J. K. *Nano Lett.* **2010**, *11* (1), 251–256.

(28) Mullins, W. W. *Acta Metall.* **1958**, *6* (6), 414–427.

(29) Zhang, Y.; Gao, T.; Gao, Y.; Xie, S.; Ji, Q.; Yan, K.; Peng, H.; Liu, Z. *ACS Nano* **2011**, *5* (5), 4014–4022.

(30) Lahiri, J.; Lin, Y.; Bozkurt, P.; Oleynik, I. I.; Batzill, M. *Nat. Nanotechnol.* **2010**, *5* (5), 326–329.

(31) Masel, R. I. *Principles of Adsorption and Reaction on Solid Surfaces*; Wiley-Interscience: New York, 1996.

(32) Li, X.; Magnuson, C. W.; Venugopal, A.; An, J.; Suk, J. W.; Han, B.; Borysiak, M.; Cai, W.; Velamakanni, A.; Zhu, Y.; Fu, L.; Vogel, E. M.; Voelkl, E.; Colombo, L.; Ruoff, R. S. *Nano Lett.* **2010**, *10* (11), 4328–4334.

(33) Dresselhaus, M. S.; Jorio, A.; Souza Filho, A. G.; Saito, R. *Philos. Trans. R. Soc., A* **2010**, *368* (1932), 5355–5377.

(34) Ferrari, A. C.; Meyer, J. C.; Scardaci, V.; Casiraghi, C.; Lazzeri, M.; Mauri, F.; Piscanec, S.; Jiang, D.; Novoselov, K. S.; Roth, S.; Geim, A. K. *Phys. Rev. Lett.* **2006**, *97* (18), 187401.

(35) Koh, Y. K.; Bae, M.-H.; Cahill, D. G.; Pop, E. *ACS Nano* **2011**, *5* (1), 269–274.

(36) Hansen, L.; Stoltze, P.; Jacobsen, K. W.; Norskov, J. K. *Phys. Rev. B* **1991**, *44* (12), 6523.

(37) Yu, Q.; Jauregui, L. A.; Wu, W.; Colby, R.; Tian, J.; Su, Z.; Cao, H.; Liu, Z.; Pandey, D.; Wei, D.; Chung, T. F.; Peng, P.; Guisinger, N. P.; Stach, E. A.; Bao, J.; Pei, S.-S.; Chen, Y. P. *Nat. Mater.* **2011**, *10* (6), 443–449.

(38) Vlassiouk, I. S., S.; Ivanov, I.; Fulvio, P. F.; Dai, S.; Meyer, H.; Chi, M.; Hensley, D.; Datskos, P.; Lavrik, N. V. *Nanotechnology* **2011**, *22* (27), 275716.

(39) Hansen, L.; Stoltze, P.; Jacobsen, K. W.; Nørskov, J. K. *Phys. Rev. B* **1991**, *44* (12), 6523.

(40) Yan, J.; Zhang, Y.; Kim, P.; Pinczuk, A. *Phys. Rev. Lett.* **2007**, *98* (16), 166802.

(41) Huang, M.; Yan, H.; Chen, C.; Song, D.; Heinz, T. F.; Hone, J. *Proc. Natl. Acad. Sci. U.S.A.* **2009**, *106* (18), 7304–7308.

(42) Pimenta, M. A.; Dresselhaus, G.; Dresselhaus, M. S.; Cancado, L. G.; Jorio, A.; Saito, R. *Phys. Chem. Chem. Phys.* **2007**, *9* (11), 1276–1290.

(43) Yu, Y.-J.; Zhao, Y.; Ryu, S.; Brus, L. E.; Kim, K. S.; Kim, P. *Nano Lett.* **2009**, *9* (10), 3430–3434.

(44) Malard, L. M.; Pimenta, M. A.; Dresselhaus, G.; Dresselhaus, M. S. *Phys. Rep.* **2009**, *473* (5−6), 51–87.

(45) Chen, S.; Brown, L.; Levendorf, M.; Cai, W.; Ju, S.-Y.; Edgeworth, J.; Li, X.; Magnuson, C. W.; Velamakanni, A.; Piner, R. D.; Kang, J.; Park, J.; Ruoff, R. S. *ACS Nano* **2011**, *5* (2), 1321–1327.

(46) Bunch, J. S.; Verbridge, S. S.; Alden, J. S.; van der Zande, A. M.; Parpia, J. M.; Craighead, H. G.; McEuen, P. L. *Nano Lett.* **2008**, *8* (8), 2458–2462.

(47) Starodub, E.; Bartelt, N. C.; McCarty, K. F. *J. Phys. Chem. C* **2010**, *114* (11), 5134–5140.

(48) Reddy, K. M.; Gledhill, A. D.; Chen, C.-H.; Drexler, J. M.; Padture, N. P. *Appl. Phys. Lett.* **2010**, *98* (11), 113117–3.

(49) Ishihara, M.; Koga, Y.; Kim, J.; Tsugawa, K.; Hasegawa, M. *Mater. Lett.* **2011**, *65* (19−20), 2864–2867.

(50) Chen, S. C., W.; Piner, R. D.; Suk, J. W.; Wu, Y.; Ren, Y.; Kang, J.; Ruoff, R. S. *Nano Lett.* **2011**, *11*, 3519–3525.

■ NOTE ADDED IN PROOF

During the review process, we became aware of two related works (refs 49 and 50). Reference 49 performs similar measurements on Cu, whereas ref 50 performs similar measurements on Cu−Ni alloy.